

# Boundary-integral method for drop deformation between parallel plates

P. J. A. Janssen and P. D. Anderson<sup>a)</sup>

*Materials Technology, Dutch Polymer Institute, Eindhoven University of Technology, P.O. Box 513, 5600 MB Eindhoven, The Netherlands*

(Received 19 October 2006; accepted 7 February 2007; published online 12 April 2007)

A new boundary-integral method is proposed to study the deformation of drops between two parallel walls. The free-space Green's functions are extended to obey the no-slip condition at the walls. The current formulation is limited to drops with viscosity equal to the matrix fluid, but can be extended to study the effect of nonunit viscosity ratio systems. With this method, the influence of the capillary number and the degree of confinement on drop deformation is investigated. Results for small capillary are compared with small-deformation theory and large capillary results with recent experiments. In both cases, an excellent match is observed. Drops undergoing shear flow deform stronger and align themselves more in the flow direction as the distance between the walls becomes smaller relative to the drop size. Furthermore, the shapes of the drops start to divert significantly from the normal ellipsoidal shapes found, as they show more pointed tips closer to the walls. The transient deformation behavior for more confined systems shows that the drops stretch out to a maximum value, and they slowly retract again to a steady situation. For larger capillary numbers even damped, oscillatory behavior is observed. Investigating the critical capillary number reveals that a minimum is found at a mediocre degree of confinement, after which the critical capillary number increases again to values even larger than the unconfined system. The breakup mode also makes a significant change as it goes from binary to ternary breakup, where the breakup occurs as the drop is retracting. © 2007 American Institute of Physics. [DOI: 10.1063/1.2715621]

## I. INTRODUCTION

Studying the nature of flow in confined geometries has become increasingly important due to downsizing of equipment.<sup>1,2</sup> Many applications for microfluidic devices consider multiphase systems. For this, T-junctions and other flow-focusing devices have been used to create dispersions with a desired drop-size distribution.<sup>3-6</sup>

The behavior of drops and blends in bulk flow has been reviewed various times.<sup>7-11</sup> In microfluidic applications, however, where the drop diameter is typically in the order of the channel height, the flow behavior can be significantly altered by the presence of channel walls. An example includes the behavior of blends and single drops undergoing shear flow in a confined system. Migler and co-workers showed the development of stable strings due to coalescence of drops, which were then stabilized due to wall and shear effects,<sup>12</sup> the development of layered structures,<sup>13</sup> and other structures not observed in bulk flow, as squashed drops.<sup>14</sup> Vananroye *et al.*<sup>15</sup> found similar results, but for lower viscosity ratios. The same authors also found that the confinement has a substantial effect on the critical capillary number.<sup>16</sup> Compared with bulk flow, drops were found harder to break up when the viscosity ratio was low. For equal viscosities, no significant effect was found. In addition, highly viscous drops were found easier to break and even drops with a viscosity ratio well above 4 could be broken, something that is impossible in bulk shear flow.<sup>17</sup> Sibillo *et al.*<sup>18</sup> investigated drops in highly confined systems, and found oscillatory be-

havior in drop deformation for high, but subcritical, capillary numbers, and complex breakup modes for supercritical capillary numbers.

Contrary to all these experimental observations, the numerical and theoretical studies have been quite limited so far. Theoretical work to include the effect of two parallel walls on the motion of, and the drag force acting upon, nearly spherical drops has been conducted by Shapria and Haber.<sup>19,20</sup> Studies for two-dimensional (2D) channel flows have been conducted to examine the migration of deformable drops,<sup>21</sup> the behavior of concentrated blends,<sup>22</sup> and the influence of surfactants and inertia.<sup>23</sup>

In this study, we use a three-dimensional boundary-integral method<sup>24,25</sup> to study the evolution of the shape of a single drop placed between two parallel plates. Boundary-integral methods have been successfully used in the past to study drop deformation in bulk flow,<sup>26-32</sup> or recently for drops squeezing through interparticle constrictions,<sup>33</sup> and have proved to provide highly accurate deformation dynamics. The inclusion of the walls, or other solid objects, is a nontrivial task in a boundary-integral method. Coulliette and Pozrikidis<sup>34,35</sup> considered the flow of a drop through a cylindrical tube, and discretized the walls as an extra surface to take into account the wall effects. The solid particle contribution was handled by a Hebecker representation<sup>36</sup> by Zinchenko and Davis.<sup>33</sup> Staben *et al.*<sup>37-39</sup> used the Green's functions associated with a parallel plate configuration, derived by Liron and Mochon,<sup>40</sup> and studied the movement of solid spheres and spheroids through channels. Those same Green's functions were also used to examine the movement and deformation of drops in a Poiseuille flow.<sup>41</sup> We have

<sup>a)</sup>Electronic mail: p.d.anderson@tue.nl

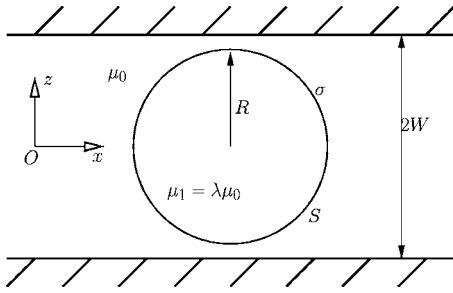


FIG. 1. Schematic representation of a drop in a matrix fluid between two parallel plates.

used a similar approach in this work. However, we have used the formulation for the Green's functions as derived by Jones,<sup>42</sup> which results in a convenient symmetric form and does not impose special demands on the location of the pole and the integration point relative to each other. Furthermore, in a similar fashion to Staben *et al.*,<sup>37</sup> we subtract slow decaying terms and handle them analytically to speed up the computations of the Green's functions.

This paper is organized as follows. In Sec. II, the mathematical formulation and numerical implementation will be discussed. In Sec. III, the influence of the confinement on drop deformation will be shown. We will mainly focus on relaxation of drops between parallel plates, and deformation and breakup in shear flow. Final conclusions will be drawn in Sec. IV.

## II. METHODS

We consider a Newtonian, inertialess drop with radius  $R$  in a Newtonian matrix fluid, located between two parallel walls. The viscosity ratio between the drop and the matrix is  $\lambda$ . In this study, we limit ourselves to cases in which the drop and the matrix have the same viscosity, i.e.,  $\lambda=1$ . The origin of the coordinate system is located exactly halfway between the two walls, so the walls are located at  $z=\pm W$ , as schematically depicted in Fig. 1. The location of the origin is nontrivial, as will be discussed below. All lengths are scaled with  $R$  and time with  $\dot{\gamma}$ , the shear rate. The walls introduce one additional parameter: the confinement ratio  $R/W$ .

A boundary-integral method<sup>24,25</sup> is used to obtain the velocity of the interface, where the velocity  $\mathbf{u}$  at the pole  $\mathbf{x}_0=(x_0, y_0, z_0)^T$  is given by

$$(\lambda + 1)\mathbf{u}(\mathbf{x}_0) = 2\mathbf{u}_\infty(\mathbf{x}_0) - \frac{1}{4\pi} \int_S \mathbf{f}(\mathbf{x}) \cdot \mathbf{G}(\mathbf{x}, \mathbf{x}_0) dS(\mathbf{x}) - \frac{\lambda - 1}{4\pi} \int_S \mathbf{u}(\mathbf{x}) \cdot \mathbf{T}(\mathbf{x}, \mathbf{x}_0) \cdot \mathbf{n}(\mathbf{x}) dS(\mathbf{x}), \quad (1)$$

where  $\mathbf{u}_\infty$  is the prescribed flow field, and  $S$  includes all the fluid interfaces in the domain. The kinematic condition at the interface reads

$$\frac{d\mathbf{x}}{dt} = \mathbf{u}(\mathbf{x}, t). \quad (2)$$

Observe that  $\mathbf{u} \neq (u, v, w)$ , as  $u$ ,  $v$ , and  $w$  are used for other expressions in Appendix A. The stress jump across the interface  $\mathbf{f}$  is given by

$$\mathbf{f}(\mathbf{x}) = \frac{1}{Ca} 2\kappa(\mathbf{x})\mathbf{n}(\mathbf{x}), \quad (3)$$

where  $Ca$  is the capillary number,  $Ca = \dot{\gamma}\mu R/\sigma$ ,  $\sigma$  is the interfacial tension, and  $\kappa$  is the local curvature, defined as  $\kappa = 1/2\nabla_s \cdot \mathbf{n}$ , with  $\nabla_s$  the surface gradient operator,  $\nabla_s = (\mathbf{I} - \mathbf{n}\mathbf{n}) \cdot \nabla$ .

In Eq. (1),  $\mathbf{G}$  and  $\mathbf{T}$  represent the Green's functions for velocity and stress, respectively, associated with the flow due to a point force. In the case of an unbounded regime, they are given by

$$\mathbf{G}^\infty(\mathbf{x}, \mathbf{x}_0) = \frac{\mathbf{I}}{|\hat{\mathbf{x}}|} + \frac{\hat{\mathbf{x}}\hat{\mathbf{x}}}{|\hat{\mathbf{x}}|^3}, \quad \mathbf{T}^\infty(\mathbf{x}, \mathbf{x}_0) = -6 \frac{\hat{\mathbf{x}}\hat{\mathbf{x}}\hat{\mathbf{x}}}{|\hat{\mathbf{x}}|^5}, \quad (4)$$

with  $\hat{\mathbf{x}} = \mathbf{x} - \mathbf{x}_0$ . Here,  $\mathbf{x} = (x, y, z)^T$  is the field point. To include the effects of the walls, we have used modified Green's functions, so  $\mathbf{G} = \mathbf{G}^\infty + \mathbf{G}^{2W}$ , where  $\mathbf{G}^{2W}$  includes all corrections due to the presence of two walls. Contrary to Staben *et al.*,<sup>37</sup> who used the Green's functions derived by Liron and Mochon,<sup>40</sup> we have used those derived by Jones.<sup>42</sup> For completeness, these functions are reproduced here,

$$G_{xx}^{2W} = -\frac{1}{2} \int_0^\infty \left( J_0(qs) + \frac{\hat{y}^2 - \hat{x}^2}{s^2} J_2(qs) \right) t_{1pp}(q, z, z_0) dq + \int_0^\infty J_0(qs) r_{1pp}(q, z, z_0) dq, \quad (5)$$

$$G_{zz}^{2W} = \int_0^\infty J_0(qs) t_{1nn}(q, z, z_0) dq, \quad (6)$$

$$G_{xy}^{2W} = \frac{\hat{x}\hat{y}}{s^2} \int_0^\infty J_2(qs) t_{1pp}(q, z, z_0) dq, \quad (7)$$

$$G_{xz}^{2W} = -\frac{\hat{x}}{s} \int_0^\infty J_1(qs) t_{1pn}(q, z, z_0) dq, \quad (8)$$

$$G_{zx}^{2W} = -\frac{\hat{x}}{s} \int_0^\infty J_1(qs) t_{1np}(q, z, z_0) dq, \quad (9)$$

with  $s = \sqrt{\hat{x}^2 + \hat{y}^2}$ ,  $\hat{x} = x - x_0$ ,  $\hat{y} = y - y_0$ , and  $J_\nu$  is the Bessel function of the first kind with order  $\nu$ . The integrands  $t_{1nn}, \dots, r_{1pp}$  can be found in Appendix A, rewritten in more convenient formulations. As can be found in Jones,<sup>42</sup> the component  $G_{yy}^{2W}$  is the same as  $G_{xx}^{2W}$ , with the change  $\hat{x} \rightarrow \hat{y}$ ,  $\hat{y} \rightarrow -\hat{x}$ ,  $G_{yz}^{2W}$  is the same as  $G_{xz}^{2W}$  with the factor  $\hat{x}$  replaced by  $\hat{y}$ ; the same change goes for  $G_{zx}^{2W}$ . Finally, by symmetry, it follows that  $G_{yx}^{2W} = G_{xy}^{2W}$ . The expression for  $G_{xy}^{2W}$  is corrected with  $1/s^2$ , which we found to be missing in the original paper [Jones (personal communication)], and we have made some minor changes in notation.<sup>43</sup>

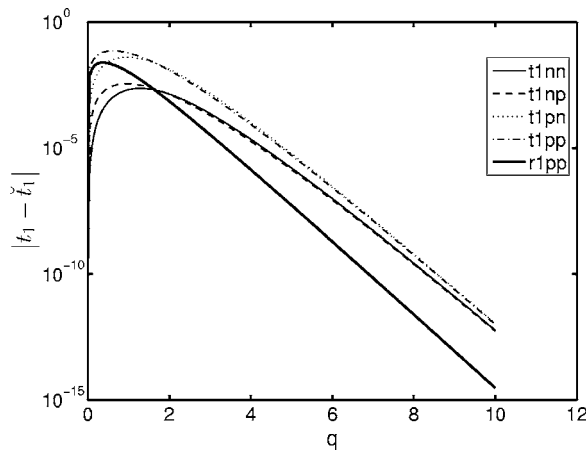


FIG. 2. Absolute value of  $t_1 - \tilde{t}_1$  as a function of  $q$ , with  $z=1$ ,  $z_0=0.2$ , and  $W=1.1$ .

All these Green's functions, as well as those derived by Liron and Mochon,<sup>40</sup> consist of infinite integrals with Bessel function weights. The main difference in the way these expressions were derived lies in the fact that Liron and Mochon placed the origin of the coordinate system at the bottom wall, whereas Jones defined it halfway between the walls. The latter approach yields a more symmetric expression.

Since the calculation of the Green's functions includes cumbersome integrals over quite complicated functions, we have modified the formulation in a similar way as has been done by Staben *et al.*<sup>37</sup> to reduce the computational effort. For high  $q$ , some approximations can be made to simplify the expressions. For example,  $E_+$ , found in Appendix A, can be approximated at high  $q$  by

$$E_+ = \frac{1}{\sinh(Wq)\cosh(Wq) + Wq} \approx 4e^{-2Wq}. \quad (10)$$

The high  $q$  approximations for all functions  $t_{1nn}, \dots, r_{1pp}$  are given in Appendix B, indicated with  $\tilde{t}_{1nn}, \dots, \tilde{r}_{1pp}$ . Using these high  $q$  approximations, we change the integration from the original formulation into

$$G_{zz}^{2W} \approx \int_0^\xi J_0(qs) \times (t_{1nn} - \tilde{t}_{1nn}) dq + \int_0^\infty J_0(qs) \tilde{t}_{1nn} dq, \quad (11)$$

with  $\xi$  typically in the order of 10. The advantage comes from the fact that the numerical integration only goes from 0 to  $\xi$ , since  $|t_{1nn} - \tilde{t}_{1nn}|$  decays rapidly, as illustrated in Fig. 2, and the other term can be evaluated analytically.

The numerical integration is performed over  $N_q$  integration points using a composite Simpson rule integration scheme. As  $|t_1 - \tilde{t}_1|$  decays rapidly, it is advantageous to have more integration points in the first part. Therefore, we split our domain into two parts: one running from 0 to  $\zeta$ , and one from  $\zeta$  to  $\xi$ , with  $\zeta$  in the order of 2. The number of integration points was chosen to be the same in each subdomain. To check the convergence and accuracy of the integration, we have performed a test case. The field point is placed on the wall:  $(0,0,W)$ , with  $W=1.1$  in this case. From the original

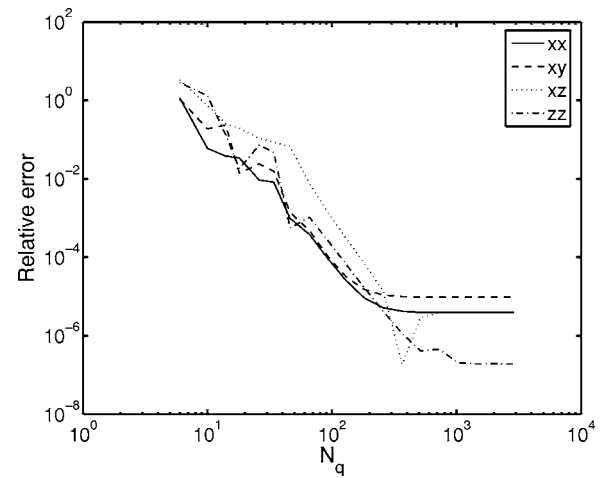


FIG. 3. The relative error in the Green's function values compared with the analytical solution as a function of the number of integration points ( $-G^\infty$ ). The parameters were  $z=W$ ,  $z_0=0.2$ ,  $\hat{x}=10$ ,  $\hat{y}=2$ , and  $W=1.1$ , and the integration domain defined by  $\zeta=1.5$  and  $\xi=7$ .

demand that the velocity should be  $\mathbf{0}$  at the wall, it follows directly that  $\mathbf{G}^{2W} = -\mathbf{G}^\infty$ . The pole is placed at  $(10, 2, 0.2)$ . This gives a value for  $s$  of 10.77, which is about the maximum value obtained in the current study. Lower values of  $s$  give fewer oscillations in the Bessel functions and hence a more accurate solution. The results are shown in Fig. 3, where the relative error of our integration, compared with the analytical solution, is plotted. As one can see, the fourth-order convergence expected from a composite Simpson integration scheme is found. The errors do not fall below  $10^{-6}$ , since that is the order of the error in the Bessel function calculation, discussed below.

As shown in Fig. 3, about 100 integration points suffice for an accurate description of the Green's function. This yields an error in the order of  $10^{-4}$ . This is still smaller than other sources of inaccuracy, most notably the curvature calculation.<sup>29</sup> In the initial stages of a simulation, as the maximum value of  $s$  is about 2 (the diameter of the drop), it was found that about 60 integration points are sufficient. The number of integration points is increased roughly linear as function of the maximum value of  $s$ , with 120 integration points at  $s=12$ . The integration domain was defined by  $\zeta=1.5$  and  $\xi=7$  for all simulations.

The total computation time can be significantly reduced by convenient storage of certain parameters in the numerical implementation. Since we integrate from 0 to  $\xi$  for every field point-pole combination with the same number of integration points, the values for  $q$  in the integration points are fixed, and the expensive hyperbolic functions only have to be calculated once for every node, and can be used for both the pole as well as for the field point. The terms  $A_+, \dots, E_-$ , as can be found in Appendix A, only depend on  $W$ , which is fixed, and thus only have to be calculated once for each integration point per simulation. If  $N_q$  is increased, these terms have to be calculated again, in total no more than five times per simulation. The factors in  $t_{1nn}, \dots, r_{1pp}$  in front of the terms in  $z$  only have to be calculated once per pole per time step, although for every integration point, which gives

$N_q N$  instead of  $N_q N^2$  evaluations, where  $N$  is the number of nodes. The Bessel functions are calculated in a discrete number of points from 0 to 200 with increments of 0.01, and subsequently stored, which also only has to be done once per simulation. The Bessel functions with argument  $sq$  during the integration are then evaluated by simple linear interpolation between two stored values, which gives an error in the order of  $10^{-6}$ , which is considered small enough for our case. The interpolation is considerably less expensive in computational effort than the complicated algorithms to accurately evaluate the Bessel functions. Finally, we make use of the reciprocity condition,

$$G_{\alpha\beta}(\mathbf{x}, \mathbf{x}_0) = G_{\beta\alpha}(\mathbf{x}_0, \mathbf{x}), \quad (12)$$

to halve the number of calculations for these Green's functions.

The boundary integral equation (1) is solved via the procedure documented in Bazhlekov *et al.*<sup>32</sup> Features of this method include the nonsingular contour integration to overcome the singularities of the kernels at  $\mathbf{x}=\mathbf{x}_0$  [see Eq. (4)], and a multi-time-step scheme, where the kernels are calculated every  $M$  time steps and all other parameters every time step. The parameter  $M$  was set to 50 in all simulations. Time steps were in the order of  $5 \times 10^{-4}$ .

The mesh is generated from a regular icosahedron, where each large triangle is then subdivided into  $n^2$  smaller ones. We used an initial mesh with 8000 triangular elements (4002 nodes) in all simulations. During the simulation, nodes are convected with an additional tangential velocity to places with high curvature to increase the local accuracy there.<sup>26</sup> For large deformations (simulations with  $Ca > 0.35$ ), this alone is not sufficient to keep a stable mesh, as the resulting slender drop shapes give an unfavorable distribution of the nodes over the drop surface. In these cases, nodes are added and redistributed using a remesh algorithm<sup>30-32</sup> that includes node subtraction and addition, topology optimization, and mesh relaxation. Remeshing is coupled with the increase in integration points. The post-breakup behavior is not investigated, so no mesh splicing is performed. The curvature is calculated with a standard contour integration method.<sup>26</sup>

The contribution of  $\mathbf{G}^{2W}$  to the total boundary integral is calculated using standard surface integration, and done separately from the free-space results, where we use the nonsingular contour integration, as mentioned above. There are no singularities in  $\mathbf{G}^{2W}$ , except when both the pole and the integration point are located on a wall, but this situation never occurs in our case, so there is no need for subtraction techniques.

In the full implementation, the computation of the additional Green's functions takes roughly 80% of the total computation time. This number is for  $N=8000$  elements and  $N_q=82$ . Increasing  $N$  will make no significant changes to this, as the biggest contribution in the remaining 20% is the computation of the free-space kernels, which also requires  $N^2$  evaluations. Increasing  $N_q$  on the other hand, this portion will go up, as the cost of evaluating  $\mathbf{G}^{2W}$  is linear in  $N_q$ . However, as  $N_q$  remains in the order of 100, no drastic changes in the relative contribution are expected. With a small time step of  $10^{-3}$ ,  $N=8000$  elements, and  $N_q=82$ ,

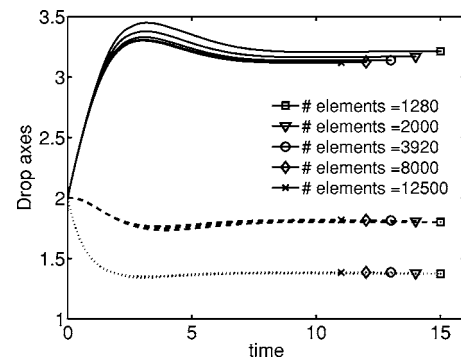


FIG. 4. Results for the drop axes in time with  $Ca=0.2$  and  $R/W=0.9$  for different meshes.

simulating one full dimensionless time unit ( $\Delta t=1$ ) takes roughly 90 min on a 2.4 GHz AMD Opteron 250 processor. So simulating from  $t=0$  to 100 takes about 6 days.

Finally, we show mesh convergence for the case with  $Ca=0.2$  and  $R/W=0.9$ . The number of elements for each mesh was 1280, 2000, 3920, 4000, and 12500, respectively. Meshes with a smaller number of elements proved to be unstable. In Fig. 4, the transient data for the three major axes of the drop can be seen. All meshes show a similar trend. As the number of elements is increased, the results converge to an identical solution. Clearly, 8000 elements are sufficient to describe the flow problem at hand.

### III. RESULTS AND DISCUSSION

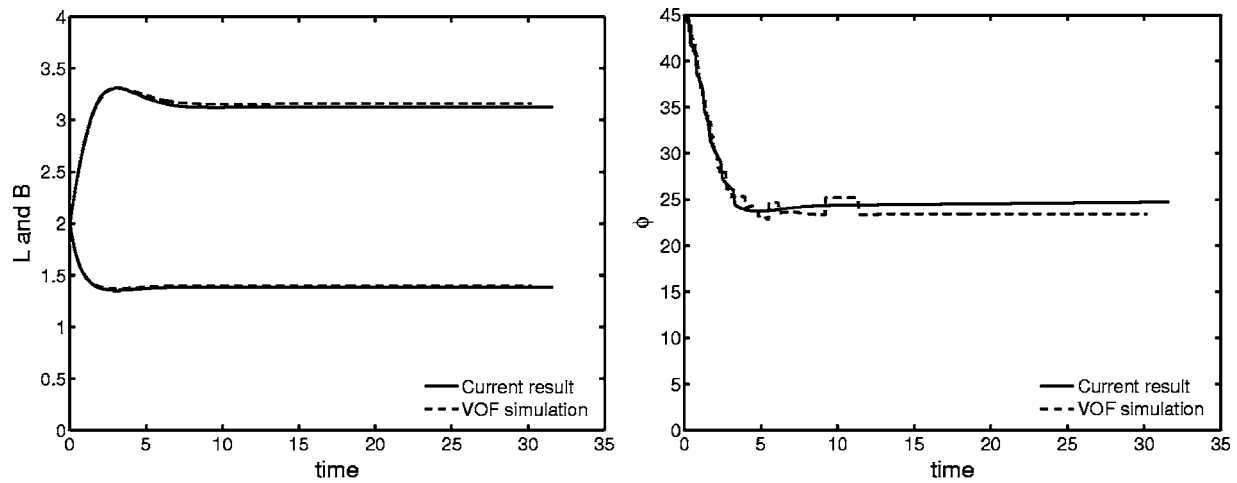
In this section, results obtained with our numerical procedure will be discussed. In the first subsection, some comparisons with other published work will be made. We will first focus on comparison with a simulation conducted with a volume-of-fluid (VOF) method. Then we will compare our results with a small-deformation theory. In the second subsection, results for various capillary numbers and confinement ratios will be shown, including those for drop retraction and drop deformation in shear flow. Finally, we investigate the influence of the confinement ratio on the critical capillary number in shear flow.

As for the Green's functions, we denote parameters and results related to the unbounded cases with the superscript  $\infty$ , the *additional* effects with the superscript  $2W$ , and the combined effects without any superscript.

#### A. Validation

First, we validate our results by comparing them with another simulation technique: a VOF-PROST<sup>44</sup> method. A drop is placed in shear flow  $[\mathbf{u}_\infty(\mathbf{x}_0)=(z_0, 0, 0)^T]$ . Figure 5 shows the results for  $Ca=0.2$  and  $R/W=0.9$ , obtained with our BIM simulation and with the VOF-PROST method by Renardy.<sup>45</sup> The axis  $L$  is defined as twice the maximum distance from the drop center to the interface,  $B$  as twice the minimum distance from center to interface, and  $L_W$  as the width in the  $xy$  plane.  $D$  is the Taylor deformation parameter,



FIG. 5. Evolution of the axes  $L$  and  $B$ , and the rotation angle in time for  $Ca=0.2$ ,  $R/W=0.9$ .

$$D = \frac{L - B}{L + B}, \quad (13)$$

and the orientation angle  $\phi$  is defined as the angle between the long axis  $L$  and the  $x$  axis.

The results for both axes as well as for the rotation angle show an excellent match. The oscillatory behavior of the deformation will be discussed in more detail later. There is a minor discrepancy in the values, but ultimate mesh convergence was not claimed for the VOF simulation. The coarseness of the mesh can influence derived quantities as  $L$  and  $B$ . Overall, the results are in excellent agreement and we are convinced our method is well capable of handling the flow problem.

Next, we compare our results with the small-deformation theory of Shapira and Haber.<sup>20</sup> In that work, the additional deformation due to the effects of the two walls was found to be [their Eq. (64) in our variables]

$$D^{2W} = Ca \left( \frac{R}{2W} \right)^3 \frac{1 + 2.5\lambda}{1 + \lambda} \frac{16 + 19\lambda}{8(1 + \lambda)} \sin(\phi) \cos(\phi) C_s, \quad (14)$$

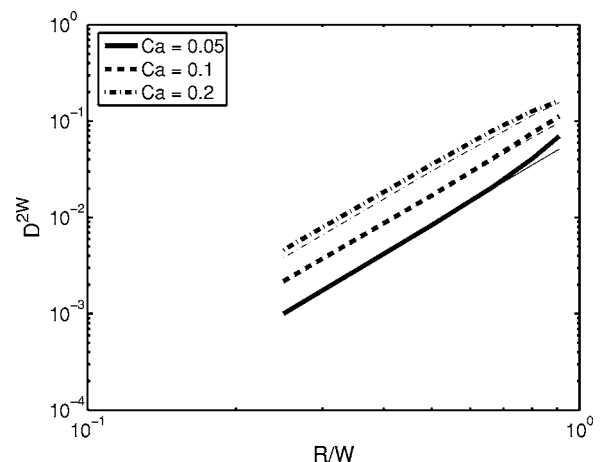
where  $C_s$  is a parameter dependent on the location of the drop in the channel, tabulated in Shapira and Haber.<sup>20</sup>

In Fig. 6, the additional deformation  $D^{2W}$  is plotted as function of the confinement ratio for cases in which the drop is placed halfway between the plates. Not only do we obtain the predicted  $(R/W)^3$  scaling, but also the absolute value gives excellent correspondence. Results for larger capillary numbers are not shown, as the drop shape significantly starts to deviate from the typical spheroidal shape, and no good matches with this theory are obtained anymore. The fact that higher confinement ratios result in nonspheroidal drops is in disagreement with the statement of Shapira and Haber:<sup>20</sup> “...wall effects have not altered the shape of the deformed droplet...” Sibillo *et al.*<sup>18</sup> also reported a good match between their experimental data and the results of Shapira and Haber.<sup>20</sup> It was also observed by these authors that there is a significant mismatch with the small-deformation theory as the confinement ratio approaches 1. Therefore, we conclude

that the validity of the small-deformation theory is only limited to small capillary numbers and small to medium confinement ratios, in other words, as long as the drops retain an almost spheroidal shape.

## B. Retraction

Next, we consider the relaxation of a deformed drop between two parallel plates. For this we first stretch a spherical drop by a factor of 2 in the  $x$  direction, and, to conserve the volume, by  $1/\sqrt{2}$  in both the  $y$  and  $z$  directions. Subsequently, the drop is placed between two parallel walls and relaxed in time. We have considered three confinement ratios (0.75, 0.9, and 1.2) and compared the relaxation behavior of the drops in those confinements with that of an unconfined drop. The results are shown in Fig. 7(a), where the major and the minor axes are shown in time. As one can see, the confinement leads to slower relaxation, as the matrix fluid has to be squeezed out between the plates and the drop, which hampers the relaxation. All drops return to a spherical shape, except for the drop with a confinement ratio of  $R/W=1.2$ . In

FIG. 6.  $D^{2W}$  as a function of  $R/W$  for three capillary numbers. The thick lines are the current results, while the thin lines correspond to the small deformation theory of Shapira and Haber (Ref. 20).

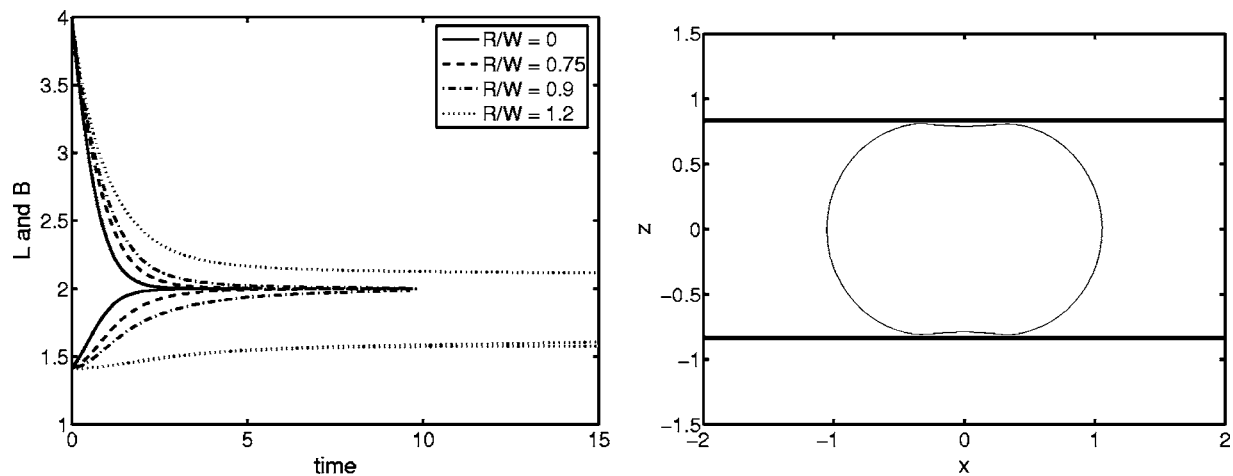


FIG. 7. (a) Evolution of  $L$  and  $B$  in time for an initially stretched drop. (b) The shape of the relaxing drop at  $y=0$  for  $R/W=1.2$  at  $t=15$ .

this case, the drop flattens against the walls, and even a dimpled shape is formed, similar to those found in film drainage in drop coalescence,<sup>46</sup> as can be seen in Fig. 7(b). Therefore, in Fig. 7(a) there are two minor axes for  $R/W=1.2$ : one corresponds with the minimum distance from the mass center to the interface, and one with the distance between two points closest to each wall. The distance between the walls, which is the asymptotic value of the  $B$  axis, is 1.67 for this case.

To handle very small wall separations, one needs to tackle singularity problems, as done, for example, by Staben *et al.*,<sup>37</sup> who computed wall separations down to 1% of the particle diameter. As a long-term study of the drainage behavior is beyond the scope of this paper, no efforts were pursued in this direction.

### C. Drop deformation in shear flow

In this section, the deformation in shear flow as a function of the capillary number and the confinement ratio is investigated. All drops are placed halfway between the two walls. In Figs. 8 and 9, the results for  $Ca=0.2$  and 0.4, respectively, are shown. The overshoot in  $D$  is typical for drop

deformation results in confined geometries. Initially the hydrodynamic interaction with the wall is strong and the drops deforms more. As the drop stretches out, it also tumbles away from the wall, so the interaction becomes less pronounced. In fact, the drop experiences a much weaker flow and starts to retract. For higher capillary numbers, a damped, oscillatory behavior can be seen, where the retracted drop rotates back, followed by an increase in deformation again. The amplitude of this deformation decreases, and eventually a stationary situation develops. Similar behavior was reported experimentally by Sibillo *et al.*<sup>18</sup> For  $Ca=0.4$  and the confinement ratios  $R/W=0.5$  and 0.67, the drop breaks up, instead of reaching a stationary shape. This will be discussed below.

For the rotation angle, we find that the angle decreases with increasing confinement ratio as the drop orients itself in the flow. The results for the orientation angle show noise due to the discrete nature of the location of the nodes. As the node associated with the maximum distance to the drop center shifts, the angle makes stepwise changes.

Some typical drop shapes are shown in Fig. 10 for  $Ca=[0.1, 0.2, 0.3, 0.4]$  and  $R/W=0.9$  in stationary situations.

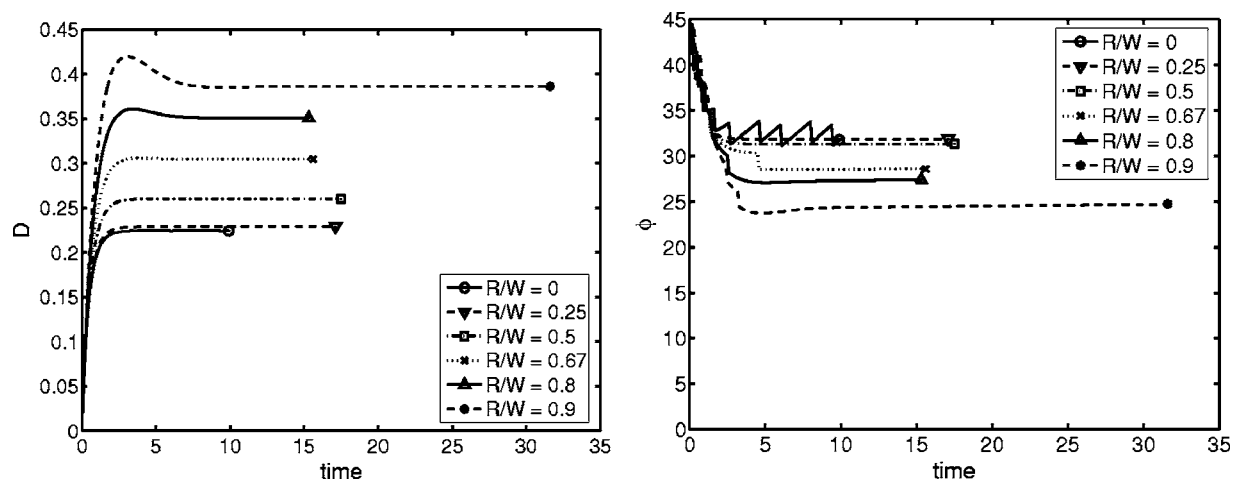
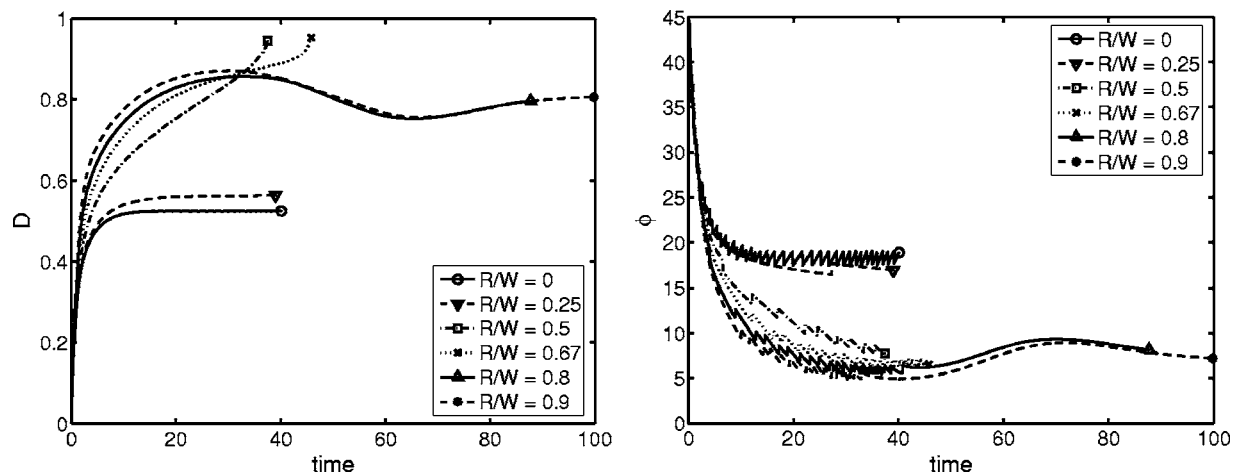


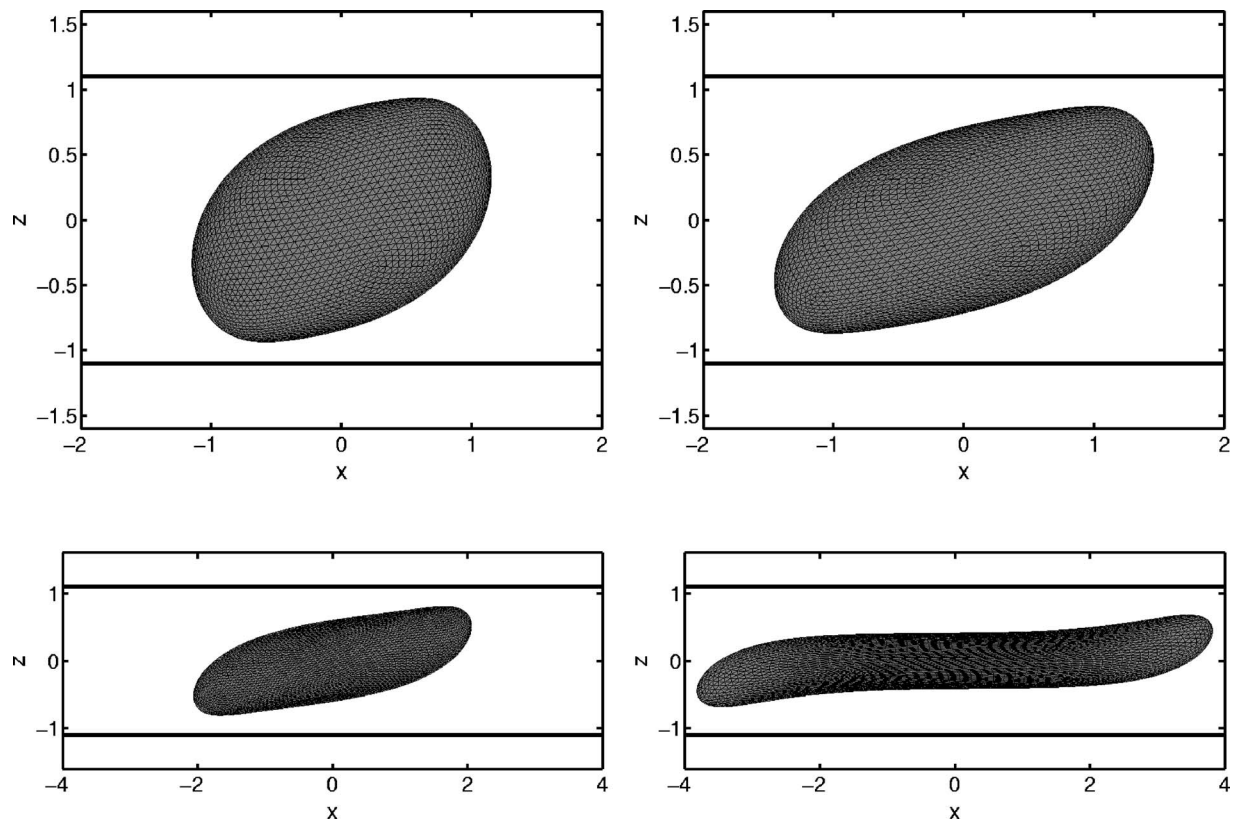
FIG. 8. Evolution of  $D$  and the rotation angle in time for  $Ca=0.2$  for various  $R/W$ .

FIG. 9. Evolution of  $D$  and the rotation angle in time for  $Ca=0.4$  for various  $R/W$ .

The drop shows stronger deformation around the tips, resulting in a nonspheroidal shape. For the higher capillary number, the drops extend significantly, resulting in greater deformation, yet no breakup. The shape can be better described as a filament, rather than as a spheroid. These findings are in agreement with the experimental work of Sibillo *et al.*<sup>18</sup> To make a direct comparison with that work, we have conducted a simulation with  $Ca=0.1$  and  $R/W=1$ . For this, the initial spherical drop was slightly compressed in the  $z$  direction and stretched in the  $x$  and  $y$  directions. After this, the shear flow was immediately applied, so the drop was not allowed to relax. These initial conditions probably do not match with

those of Sibillo *et al.*,<sup>18</sup> but are simple, prevent singularity problems, and will only have a minor influence on the eventual result. In Fig. 11, the drop shapes in time are seen at four time instances. As one can see, we obtain an excellent match with the experimental data.

Streaklines are presented in Fig. 12 for  $Ca=0.2$  and  $R/W=0$  and  $0.9$  in the stationary situation. In the case of the confined drop, high shear rates are found between the tips and the walls, where the matrix fluid is squeezed between the drop and the wall. Furthermore, a large portion of the matrix fluid does not pass between the wall and the drop, but is reversed.

FIG. 10. Stationary drop shapes for  $Ca=(a)$  0.1, (b) 0.2, (c) 0.3, and (d) 0.4 for  $R/W=0.9$ .

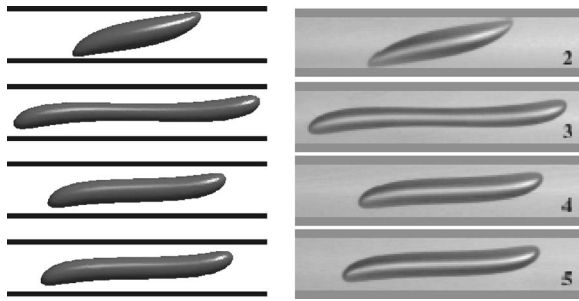


FIG. 11. Shape evolution of a drop in time with  $Ca=0.4$ ,  $R/W=1$ . The images on the right are experimental data and taken with permission from Fig. 1 of Sibillo *et al.* [Phys. Rev. Lett. **97**, 054502 (2006)]. Copyright 2006 by the American Physical Society.

#### D. Critical capillary number

Finally, we investigate the influence of confinement on the critical capillary number in shear flow,  $Ca_{crit}$ , above which the drop breaks up. All simulations were started with initially spherical drops. Simulations were run until a stationary state was reached, or until the drop broke up. The critical capillary number was determined within 0.01. The results can be seen in Fig. 13, and are also tabulated in Table I.

With increasing confinement ratio,  $Ca_{crit}$  initially decreases, and reaches a minimum at  $Ca=0.5$ , with  $Ca_{crit}=0.375$ . By further increasing the confinement ratio,  $Ca_{crit}$  increases again. For the highest confinement ratios,  $Ca_{crit}$  is even larger than the unconfined result. Vananroye *et al.*<sup>16</sup> also found a minor influence of the confinement ratio on  $Ca_{crit}$  for cases with  $\lambda \approx 1$ . An even more interesting observation is that the breakup mode makes a significant change: it changes from binary into ternary breakup. The evolution of the drop shapes for three supercritical capillary numbers ( $Ca=0.44$  for  $R/W=0.75$ ,  $Ca=0.46$  for  $R/W=0.8$ , and  $Ca=0.47$  for  $R/W=0.9$ ) is shown in Figs. 14(a)–14(c). For all cases, the drop initially stretches out and forms larger blobs at the tips that point toward the walls. As the drop starts to retract, a wave forms between the blobs. In the case of  $Ca=0.44$  with  $R/W=0.75$ , the wave has only one period. Eventually, the amplitude of the wave grows, also due to retraction, and a new blob forms in the center. The drop will eventually break up into three drops, with roughly equal size. The simulation was stopped here, as the curvature became too large. As mentioned before, no mesh splicing is conducted, so the post-breakup behavior is not investigated. For  $Ca$

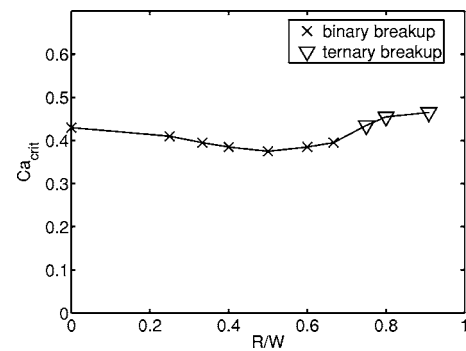


FIG. 13. The critical capillary number as a function of the confinement ratio.

$=0.46$  with  $R/W=0.8$  and  $Ca=0.47$  with  $R/W=0.9$ , we see similar behavior. However, the wave between the drops has two periods. In the later stages, the two middle parts merge into a larger one. The final shape just prior to breakup shows once again three drops forming; the middle one, however, is larger than the two outer ones. However, the middle one is also more slender than the two on the outside. So eventually also three, roughly equal sized drops will form.

In Fig. 14(d), a breakup shape reported by Sibillo *et al.*<sup>18</sup> for  $Ca=0.46$ ,  $R/W=0.7$  is shown. Similar to our results, they also found a stretched drop breaking into three fragments, all roughly equal in size. The experimental conditions are not exactly identical to the numerical, but still an excellent agreement is found.

These results show that this method can be readily applied for a more detailed study on the influence of wall effects on the critical capillary number.<sup>11,47</sup> However, to investigate the post-breakup behavior and final drop size distribution, the code needs to be extended to handle breakup.

#### IV. CONCLUSIONS

A boundary integral method is proposed to study drop deformation between two parallel plates. The Green's functions normally used are modified to include the effects of the walls. The deformation of drops with viscosity ratio 1 in shear flow is investigated as a function of the capillary number and the confinement ratio. In general, a drop placed between parallel plates shows a larger deformation than unconfined drops. Furthermore, for high confinement ratios,

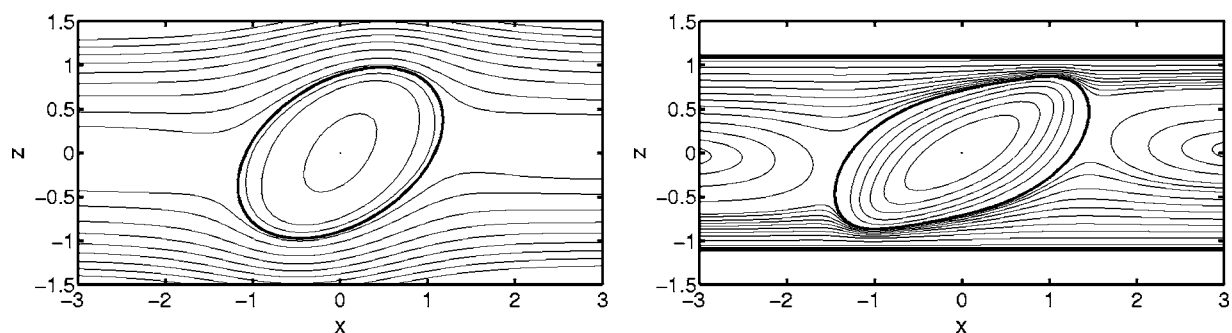


FIG. 12. Streamlines and drop shapes for  $Ca=0.2$  with (a)  $R/W=0$  and (b)  $0.9$  in the stationary situation.



TABLE I. The critical capillary number as a function of the confinement ratio.

$R/W$	0	0.25	0.33	0.4	0.5	0.6	0.66	0.75	0.8	0.9
$Ca_{crit}$	0.435	0.415	0.395	0.385	0.375	0.385	0.395	0.435	0.455	0.465

oscillatory behavior is observed, as drops tumble away, retract, rotate back, and deform again. Despite the higher deformation, there is only a minor influence on the critical capillary number. With increasing confinement ratio, the critical capillary initially decreases. It reaches a minimum at a moderate confinement ratio, and then increases again. The breakup mode, however, does make a significant change, as it changes from binary breakup into ternary breakup at high confinement ratios. This behavior is similar as observed in recent experiments.

The behavior of drops in other flow conditions, such as Poiseuille flow or oscillating shear flow, can be studied with our method. Furthermore, the method can be easily extended to include the effect of surfactants or buoyancy effects. More effort will have to be taken to extend the method to handle nonunit viscosity ratios, as the double-layer potential needs to be determined and computed as well.

## ACKNOWLEDGMENTS

This work was sponsored by the Dutch Polymer Institute (DPI), Project No. 446. We thank Professor Y. Renardy for providing us with the results of the VOF-PROST simulation.

## APPENDIX A: GREEN'S FUNCTIONS FOR PARALLEL WALLS

The Green's function for a point force in a fluid between two parallel walls was derived by Jones.<sup>42</sup> The expressions are all integrals over  $q$  with Bessel function weights. The integrands are defined as follows:

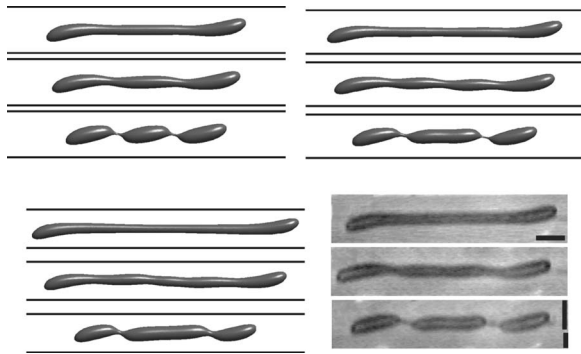


FIG. 14. Drop shapes in time for supercritical situations: (a)  $Ca=0.44$  and  $R/W=0.75$ ; (b)  $Ca=0.46$  and  $R/W=0.8$ ; (c)  $Ca=0.47$  and  $R/W=0.9$ ; (d)  $Ca=0.46$  and  $R/W=0.7$  taken with permission from Fig. 3 of Sibillo *et al.* [Phys. Rev. Lett. **97**, 054502 (2006)]. Copyright 2006 by the American Physical Society.

$$\begin{aligned}
 t_{1nn}(q, z, z_0) = & E_-[-v \cosh(v) + B_+ \sinh(v)]w \cosh(w) \\
 & + E_+[-v \sinh(v) + A_+ \cosh(v)]w \sinh(w) \\
 & + E_+[A_+ v \sinh(v) - C_+ \cosh(v)]\cosh(w) \\
 & + E_-[B_+ v \cosh(v) - D_+ \sinh(v)]\sinh(w),
 \end{aligned} \quad (A1)$$

$$\begin{aligned}
 t_{1np}(q, z, z_0) = & E_-[v \sinh(v) - A_- \cosh(v)]w \cosh(w) \\
 & + E_+[v \cosh(v) - B_- \sinh(v)]w \sinh(w) \\
 & + E_+[-A_+ v \cosh(v) + u^2 \sinh(v)]\cosh(w) \\
 & + E_-[-B_+ v \sinh(v) + u^2 \cosh(v)]\sinh(w),
 \end{aligned} \quad (A2)$$

$$\begin{aligned}
 t_{1pn}(q, z, z_0) = & E_+[-v \sinh(v) + A_+ \cosh(v)]w \cosh(w) \\
 & + E_-[-v \cosh(v) + B_+ \sinh(v)]w \sinh(w) \\
 & + E_-[A_- v \cosh(v) - u^2 \sinh(v)]\cosh(w) \\
 & + E_+[B_- v \sinh(v) - u^2 \cosh(v)]\sinh(w),
 \end{aligned} \quad (A3)$$

$$\begin{aligned}
 t_{1pp}(q, z, z_0) = & E_+[v \cosh(v) - B_- \sinh(v)]w \cosh(w) \\
 & + E_-[v \sinh(v) - A_- \cosh(v)]w \sinh(w) \\
 & + E_-[-A_- v \sinh(v) + C_- \cosh(v) \\
 & - 2u \tanh(u) \cosh(v)]\cosh(w) \\
 & + E_+[-B_- v \cosh(v) + D_- \sinh(v) \\
 & - 2u \coth(u) \sinh(v)]\sinh(w),
 \end{aligned} \quad (A4)$$

$$\begin{aligned}
 r_{1pp}(q, z, z_0) = & [-2e^{-u} \cosh(v)/\cosh(u)]\cosh(w) \\
 & + [-2e^{-u} \sinh(v)/\sinh(u)]\sinh(w),
 \end{aligned} \quad (A5)$$

where

$$u = qW, \quad v = qz_0, \quad w = qz, \quad (A6)$$

$$A_{\pm}(u) = u \pm \sinh(u)e^{-u} = u \pm 0.5(1 - e^{-2u}), \quad (A7)$$

$$B_{\pm}(u) = u \pm \cosh(u)e^{-u} = u \pm 0.5(1 + e^{-2u}), \quad (A8)$$

$$C_{\pm}(u) = u(1 + u) \pm \sinh(u)e^{-u} = u(1 + u) \pm 0.5(1 - e^{-2u}), \quad (A9)$$

$$D_{\pm}(u) = u(1+u) \pm \cosh(u)e^{-u} = u(1+u) \pm 0.5(1+e^{-2u}), \quad (\text{A10})$$

$$E_{\pm}(u) = \frac{1}{\sinh(u)\cosh(u) \pm u}. \quad (\text{A11})$$

## APPENDIX B: HIGH $q$ APPROXIMATIONS

In Sec. II, the high  $q$  approximations for  $t$ , indicated as  $\check{t}$ , are introduced. They are given by

$$\begin{aligned} \check{t}_{1nn} = & [\{-2(W-z)(W-z_0)\}q^2 + \{-2W+z+z_0\}q - 1] \\ & \times \exp([z+z_0-2W]q) + [\{-2(W+z)(W+z_0)\}q^2 \\ & + \{-2W-z-z_0\}q - 1] \exp([-z-z_0-2W]q), \end{aligned} \quad (\text{B1})$$

$$\begin{aligned} \check{t}_{1np} = & [2(W-z)(W-z_0)q^2 + \{z-z_0\}q] \\ & \times \exp([z+z_0-2W]q) + [\{-2(W+z)(W+z_0)\}q^2 \\ & + \{z-z_0\}q] \exp([-z-z_0-2W]q), \end{aligned} \quad (\text{B2})$$

$$\begin{aligned} \check{t}_{1pn} = & [\{-2(W-z)(W-z_0)\}q^2 + \{z-z_0\}q] \\ & \times \exp([z+z_0-2W]q) + [2(W+z)(W+z_0)q^2 \\ & + \{z-z_0\}q] \exp([-z-z_0-2W]q), \end{aligned} \quad (\text{B3})$$

$$\begin{aligned} \check{t}_{1pp} = & [2(W-z)(W-z_0)q^2 + \{-2W+z+z_0\}q - 1] \\ & \times \exp([z+z_0-2W]q) + [2(W+z)(W+z_0)q^2 \\ & + \{-2W-z-z_0\}q - 1] \exp([-z-z_0-2W]q), \end{aligned} \quad (\text{B4})$$

$$\check{r}_{1pp} = -2 \exp([z+z_0-2W]q) - 2 \exp([-z-z_0-2W]q). \quad (\text{B5})$$

<sup>1</sup>H. Stone, A. Stroock, and A. Ajdari, "Engineering flows in small devices: Microfluidics toward a lab-on-a-chip," *Annu. Rev. Fluid Mech.* **36**, 381 (2004).

<sup>2</sup>T. Squires and S. Quake, "Microfluidics: Fluid physics at the nanoliter scale," *Rev. Mod. Phys.* **77**, 977 (2005).

<sup>3</sup>T. Thorsen, R. Roberts, F. Arnold, and S. Quake, "Dynamic pattern formation in a vesicle-generating microfluidic device," *Phys. Rev. Lett.* **86**, 4163 (2001).

<sup>4</sup>J. Tice, A. Lyon, and R. Ismagilov, "Effects of viscosity on droplet formation and mixing in microfluidic channels," *Anal. Chim. Acta* **507**, 73 (2004).

<sup>5</sup>P. Garstecki, H. Stone, and G. Whitesides, "Mechanism for flow-rate controlled breakup in confined geometries: A route to monodisperse emulsions," *Phys. Rev. Lett.* **94**, 164501 (2005).

<sup>6</sup>P. Garstecki, M. Fuerstman, H. Stone, and G. Whitesides, "Formation of droplets and bubbles in a microfluidic T-junction—Scaling and mechanism of break-up," *Lab Chip* **6**, 437 (2006).

<sup>7</sup>J. Rallison, "The deformation of small viscous drops and bubbles in shear flows," *Annu. Rev. Fluid Mech.* **16**, 45 (1984).

<sup>8</sup>H. Stone, "Dynamics of drop deformation and breakup in viscous flows," *Annu. Rev. Fluid Mech.* **26**, 65 (1994).

<sup>9</sup>C. Tucker III and P. Moldenaers, "Microstructural evolution in polymer blends," *Annu. Rev. Fluid Mech.* **34**, 177 (2002).

<sup>10</sup>V. Cristini and Y.-C. Tan, "Theory and numerical simulation of droplet dynamics in complex flows—A review," *Lab Chip* **4**, 257 (2004).

<sup>11</sup>V. Cristini and Y. Renardy, "Scalings for drop sizes in shear-driven breakup: Non-microfluidic ways to monodisperse emulsions," *Fluid Dyn. Mater. Process.* **2**, 77 (2006).

<sup>12</sup>K. Migler, "String formation in sheared polymer blends: Coalescence, breakup, and finite size effects," *Phys. Rev. Lett.* **86**, 1023 (2001).

<sup>13</sup>J. Pathak, M. Davis, S. Hudson, and K. Migler, "Layered droplet microstructures in sheared emulsions: Finite-size effects," *J. Colloid Interface Sci.* **255**, 391 (2002).

<sup>14</sup>J. Pathak and K. Migler, "Droplet-string deformation and stability during microconfined shear flow," *Langmuir* **19**, 8667 (2003).

<sup>15</sup>A. Vananroye, P. van Puyvelde, and P. Moldenaers, "Structure development in confined polymer blends: Steady-state shear flow and relaxation," *Langmuir* **22**, 2273 (2006).

<sup>16</sup>A. Vananroye, P. van Puyvelde, and P. Moldenaers, "Effect of confinement on droplet breakup in sheared emulsions," *Langmuir* **22**, 3972 (2006).

<sup>17</sup>H. Grace, "Dispersion phenomena in high viscosity immiscible fluid systems and application of static mixers as dispersion devices in such systems," *Chem. Eng. Commun.* **14**, 225 (1982).

<sup>18</sup>V. Sibillo, G. Pasquariello, M. Simeone, V. Cristini, and S. Guido, "Drop deformation in microconfined shear flow," *Phys. Rev. Lett.* **97**, 054502 (2006).

<sup>19</sup>M. Shapira and S. Haber, "Low Reynolds number motion of a droplet between two parallel plates," *Int. J. Multiphase Flow* **14**, 483 (1988).

<sup>20</sup>M. Shapira and S. Haber, "Low Reynolds number motion of a droplet in shear flow including wall effects," *Int. J. Multiphase Flow* **16**, 305 (1990).

<sup>21</sup>S. Mortazavi and G. Tryggvason, "A numerical study of the motion of drops in Poiseuille flow. Part 1. Lateral migration of one drop," *J. Fluid Mech.* **411**, 325 (2000).

<sup>22</sup>X. Li and C. Pozrikidis, "Wall-bounded shear flow and channel flow of suspensions of liquid drops," *Int. J. Multiphase Flow* **26**, 1247 (2000).

<sup>23</sup>J. Lee and C. Pozrikidis, "Effect of surfactants on the deformation of drops and bubbles in Navier-Stokes flow," *Comput. Fluids* **35**, 43 (2006).

<sup>24</sup>J. Rallison and A. Acrivos, "A numerical study of the deformation and burst of a viscous drop in an extensional flow," *J. Fluid Mech.* **89**, 191 (1978).

<sup>25</sup>C. Pozrikidis, *Boundary-Integral and Singularity Methods for Linearized Viscous Flow* (Cambridge University Press, Cambridge, 1992).

<sup>26</sup>M. Loewenberg and E. Hinch, "Numerical simulation of concentrated emulsion in shear flow," *J. Fluid Mech.* **321**, 395 (1996).

<sup>27</sup>M. Loewenberg and E. Hinch, "Collision of two deformable drops in shear flow," *J. Fluid Mech.* **338**, 299 (1997).

<sup>28</sup>M. Rother, A. Zinchenko, and R. Davis, "Buoyancy-driven coalescence of slightly deformable drops," *J. Fluid Mech.* **346**, 117 (1997).

<sup>29</sup>A. Zinchenko, M. Rother, and R. Davis, "A novel boundary-integral algorithm for viscous interaction of deformable drops," *Phys. Fluids* **9**, 1493 (1997).

<sup>30</sup>V. Cristini, J. Blawdziewicz, and M. Loewenberg, "Drop breakup in three-dimensional viscous flows," *Phys. Fluids* **10**, 1781 (1998).

<sup>31</sup>V. Cristini, J. Blawdziewicz, and M. Loewenberg, "An adaptive mesh algorithm for evolving surfaces: Simulation of drop breakup and coalescence," *J. Comput. Phys.* **168**, 445 (2001).

<sup>32</sup>I. Bazhlekova, P. Anderson, and H. Meijer, "Non-singular boundary-integral method for deformable drops in viscous flows," *Phys. Fluids* **16**, 1064 (2004).

<sup>33</sup>A. Zinchenko and R. Davis, "A boundary-integral study of a drop squeezing through interparticle constrictions," *J. Fluid Mech.* **564**, 227 (2006).

<sup>34</sup>C. Coulliette and C. Pozrikidis, "Flow due to a periodic array of point forces and the motion of small particles within a cylindrical tube of arbitrary cross section," *Phys. Fluids* **8**, 2019 (1996).

<sup>35</sup>C. Coulliette and C. Pozrikidis, "Motion of an array of drops through a cylindrical tube," *J. Fluid Mech.* **358**, 1 (1998).

<sup>36</sup>F.-K. Hebeker, "Efficient boundary element methods for three-dimensional exterior viscous flows," *Numer. Methods Partial Differ. Equ.* **2**, 273 (1986).

<sup>37</sup>M. Staben, A. Zinchenko, and R. Davis, "Motion of a particle between two parallel plane walls in low-Reynolds-number Poiseuille flow," *Phys. Fluids* **15**, 1711 (2003).

<sup>38</sup>M. Staben, K. Galvin, and R. Davis, "Low-Reynolds-number motion of a heavy sphere between two parallel plane walls," *Chem. Eng. Sci.* **61**, 1932 (2006).

- <sup>39</sup>M. Staben, A. Zinchenko, and R. Davis, "Dynamic simulation of spheroid motion between two parallel plane walls in low-Reynolds-number Poiseuille flow," *J. Fluid Mech.* **553**, 187 (2006).
- <sup>40</sup>N. Liron and S. Mochon, "Stokes flow for a Stokes-let between 2 parallel flat plates," *J. Eng. Math.* **10**, 287 (1976).
- <sup>41</sup>A. Griggs, A. Zinchenko, and R. Davis, "Low-Reynolds-number motion of a deformable drop between two parallel plane walls," *Int. J. Multiphase Flow* **33**, 182 (2007).
- <sup>42</sup>R. Jones, "Spherical particle in Poiseuille flow between planar walls," *J. Chem. Phys.* **121**, 483 (2004).
- <sup>43</sup>We changed the notation used in Jones from  $\mathbf{T}_1$  into  $\mathbf{G}^{2W}$  to maintain  $\mathbf{T}$  as the notation for the stresslet, which is common in BIM,  $x$  and  $y$  were changed into  $\hat{x}$  and  $\hat{y}$ , respectively, and  $z_1$  and  $z_2$  into  $z$  and  $z_0$ .
- <sup>44</sup>Y. Renardy and M. Renardy, "PROST: A parabolic reconstruction of surface tension for the volume-of-fluid method," *J. Comput. Phys.* **183**, 400 (2002).
- <sup>45</sup>Y. Renardy, "The effects of confinement and inertia on the production of droplets," *Rheol. Acta* **46**, 521 (2007).
- <sup>46</sup>A. Chesters, "The modelling of coalescence of fluid-liquid dispersions: A review of current understanding," *Trans. Inst. Chem. Eng., Part A* **69**, 259 (1991).
- <sup>47</sup>V. Cristini, S. Guido, A. Alfani, J. Bławdziewicz, and M. Loewenberg, "Drop breakup and fragment size distribution in shear flow," *J. Rheol.* **47**, 1283 (2003).